PLOS ONE

RESEARCH ARTICLE

The effect of Fe_2O_3 crystal phases on CO_2 hydrogenation

Wensheng Ning[1]*, Tianqi Wang[1], Hongxian Chen[1], Xiazhen Yang[1], Yangfu Jin[2]

1 College of Chemical Engineering, Zhejiang University of Technology, Hangzhou, China, **2** College of Materials Science and Technology, Zhejiang University of Technology, Hangzhou, China

* wenshning@sohu.com

Citation: Ning W, Wang T, Chen H, Yang X, Jin Y (2017) The effect of Fe_2O_3 crystal phases on CO_2 hydrogenation. PLoS ONE 12(8): e0182955. https://doi.org/10.1371/journal.pone.0182955

Editor: Yogendra Kumar Mishra, Institute of Materials Science, GERMANY

Received: April 17, 2017

Accepted: July 27, 2017

Published: August 14, 2017

Data Availability Statement: All relevant data are within the paper and its Supporting Information files.

Funding: This work was supported by the Zhejiang Provincial Natural Science Foundation of China (LY14B030003) and the National Ministry of Science and Technology of China (2014BAD02B05). The funders had no role in study design, data collection and analysis, decision to publish, or preparation of the manuscript.

Competing interests: The authors have declared that no competing interests exist.

Abstract

The effect of Fe_2O_3 crystal phases on their performance in CO_2 hydrogenation was studied. α-Fe_2O_3 crystal was prepared by precipitation method from $Fe(NO_3)_3{\cdot}9H_2O$ and $(NH_4)_2CO_3$, and γ-Fe_2O_3 was prepared by grinding $Fe(NO_3)_3{\cdot}9H_2O$ and L(+)-Tartaric acid in agate mortar completely. The crystal phases of Fe_2O_3 influence the distribution of promoter Zn, K and Cu on catalysts. The dispersity of K on γ-Fe_2O_3 surface is higher than α-Fe_2O_3. On the contrary, Cu and Zn are more dispersive on α-Fe_2O_3 surface than γ-Fe_2O_3. The catalyst in γ-Fe_2O_3 phase is easily reduced relative to the catalyst in α-Fe_2O_3 phase. The former presents higher CO_2 conversion and C_2+ hydrocarbon selectivity than the latter in CO_2 hydrogenation.

Introduction

CO_2 hydrogenation for organic chemicals is a worthy study under the background that CO_2 used as raw material for chemicals other than discharged into atmosphere would be helpful to abate the greenhouse effect. However, the difficulty to capture CO_2 and the cost to supply H_2 make most of the researches stayed in laboratory. The concept and trial using seawater as starting materials brings an applicable and profitable scene to CO_2 hydrogenation [1–4]. Seawater is a natural absorbent of CO_2, from which plenty of CO_2 can be captured. Seawater is an unlimited source for H_2, too. The above concept becomes accepted to us because the device to transfer solar power into electricity can be constructed on the vast ocean, which would supply enough energy to produce CO_2 and H_2 from seawater simultaneously. With the concept breakthrough where and how to perform CO_2 hydrogenation, active catalysts are the key component to commercialize CO_2 hydrogenation.

The organic chemicals synthesized from CO_2 hydrogenation include methane, methanol, methyl acid, dimethyl ether, hydrocarbons and mixed alcohols [5–7]. Among them, hydrocarbons are a good product because it can be upgraded into liquid fuels which are cleaner than the petroleum-based fuels [8]. It is accepted that CO_2 is hydrogenated into hydrocarbons by two steps: CO is produced from CO_2 by reverse Water-Gas shift (WGS) reaction (Reaction I), then the CO reacts with H_2 to synthesize hydrocarbons via Fischer-Tropsch synthesis (FTS)

(Reaction II) [9–14].

$$\text{Reaction I}: \ CO_2 + H_2 = CO + H_2O$$

$$\text{Reaction II}: \ CO + 2H_2 = (CH_2) + H_2O$$

Fe and Co are commercial catalysts for FTS. Riedel et al. [15] compared the performance of Fe and Co catalysts in the mixtures of CO, CO_2, and H_2. With increased CO_2 and decreased CO content in the feedgas, the product composition shifted from a mixture of mainly higher hydrocarbons to almost exclusively methane for Co catalyst, while Fe catalyst synthesized the same hydrocarbon products from CO_2 /H_2 as from CO/H_2 syngas. Zhang et al. [16] also found that the CO_2 hydrogenation products contained about 70% or more methane for supported Co catalyst. These distinctions are partly attributed to that Fe catalyst is active for both of the Reaction I and II [15,17,18].

In order to improve the performance of Fe catalysts in CO_2 hydrogenation, the effects of promoter [8,10,13,15,19–24], supporter [15,20,22,24,25], preparation method [8,13,15,21–26] and reducing agent [8] are studied very much. In these studies, iron oxide almost presents in α-Fe_2O_3 [15,21,26] or Fe_3O_4 [25] crystal phase in the as-prepared catalysts. Considering that γ-Fe_2O_3 is one kind of iron oxide as common as α-Fe_2O_3 [27,28], it is surprising that there are very few reports about the behavior of γ-Fe_2O_3 in CO_2 hydrogenation. Al-Dossary et al. found γ-Fe_2O_3 coexisted with α-Fe_2O_3 in the catalysts, but no benefit from γ-Fe_2O_3 was disclosed [21]. However, it has been confirmed that γ-Fe_2O_3 is superior to α-Fe_2O_3 in other catalytic reactions, such as photodecomposition of H_2S [29], selective catalytic reduction of NO_X with NH_3 [30], electroanalysis and ultrasensitive detection of Pb^{2+} [27], WGS reaction [31] and so on. The lack on the performance of γ-Fe_2O_3 in CO_2 hydrogenation makes it necessary to study Fe catalyst in γ-Fe_2O_3 phase, not only to supply the knowledge about γ-Fe_2O_3 in the reaction, but also to find active catalyst to make CO_2 profitable.

We has reported the influences of Fe_2O_3 crystal phases on CO_2 hydrogenation [32]. γ-Fe_2O_3 phase in the catalysts was formed by washing FeAl precipitate with anhydrous ethanol. The catalyst with strong γ-Fe_2O_3 phase was more active in the reaction than the catalysts with none or weak γ-Fe_2O_3 phase. In order to avoid the possible promotion of Al on the catalyst activity and prepare the catalyst in pure γ-Fe_2O_3 phase simultaneously, solid-phase reaction was used recently for catalyst preparation. The effect of Fe_2O_3 phase on the catalyst reactivity is explored in this work.

Materials and methods

Catalyst preparation

Three kinds of catalyst precursor were prepared. P-1 was prepared by precipitating Fe$(NO_3)_3 \cdot 9H_2O$ solution with $(NH_4)_2CO_3$ solution under vigorous stirring at 50˚C and pH = 6.5. The resulting precipitate was aged at 50˚C for 0.5 h and room temperature for 1 h. After it was washed with distilled water and centrifuged for three times, the precipitate was dried at 120˚C overnight and calcined at 500˚C for 6 h in static air [32]. P-2 was prepared by grinding Fe$(NO_3)_3 \cdot 9H_2O$ and L(+)-Tartaric acid (1:1 in mass ratio) in agate mortar completely. The obtained deep red solid was washed with dehydrated alcohol for three times. Then, the solid was dried at 80˚C for 3 h and calcined at 400˚C for 1 h. P-3 was prepared in the same procedure as P-2 except some water was added during the grinding. The precursors were shaped into particles of 150–280 μm and impregnated with Zn, K and Cu in the mass ratio of 2%, 3% and 4%, respectively. After the impregnated precursors were dried at 120˚C for 12 h, the impregnated P-1 was calcined at 500˚C for 6 h, while the impregnated

P-2 and P-3 were calcined at 400˚C for 1 h. The promoted catalysts were named as C-1, C-2 and C-3 correspondingly.

Characterization

The crystal structure of the catalysts was acquired by X-ray diffraction (XRD, PNAlytical X'Pert Pro diffractometer) with a Cu K_α radiation source (λ = 0.15406 nm) in reflection mode. X-ray tube was operated at 40 kV and 40 mA. Surface area and pore structure of the samples were measured by ASAP-2020 from Micromeritics at liquid nitrogen temperature. Temperature-programmed reduction (TPR) was carried out in PX200 (Tianjin Pengxiang LTD.) with 5% H_2/N_2 of 30 mL/min and a TCD detector. The sample was heated to 850˚C at the rate of 10˚C/min. The morphology of the catalysts was observed by scanning electron microscopy (SEM, Hitachi S-4700II) which was attached with an energy dispersive spectroscopy (EDS, Thermo NORAN VANTAGE ESI.).The accelerating voltage is 15 kV. The results from SEM and EDS are shown in S1 and S2 Figs, respectively. XPS analysis was done at Catalysis and Surface Science End-station of National Synchrotron Radiation Laboratory in University of Science & Technology of China using Mg K_α radiation (1253.6 eV) and VG SCIENTA R4000 analyzer. The binding energy of C 1s (285.0 eV) was used to calibrate the peak position of other elements.

Activity test and product analysis

The reactivity of catalysts was tested in a stainless steel fixed bed reactor of inter-diameter of 8 mm [19]. A 1.0 g catalyst (150–280 μm) was mixed with 4.0 g quartz sand and they were filled into the reactor. After the catalyst was reduced in CO of 3.0 L/(h·g-cat) at 300˚C for 6 h, it was cooled to room temperature. Then, the feed gas was changed into mixed gases of H_2:CO_2:N_2 = 16:8:1 of 1.6 MPa and 6.0 L/(h·g-cat). The catalyst was heated to 230˚C in about 3 h for activity evaluation of 45 h. The condensable products were collected in a cold trap of 0˚C at system pressure. After the system pressure was released through a backpressure regulator, the exited gas was analyzed by GC A90 (Shanghai Yimeng LTD.) on line. The quantities of CO, CH_4, CO_2 and N_2 were supplied with TCD detector and TDX-01 column. C_1–C_4 hydrocarbons were analyzed with FID detector and Porapak Q column.

Results and discussion

Crystal phase of the precursors and catalysts

Fig 1 shows the XRD patterns of precursor P-1, P-2 and P-3. There is only α-Fe_2O_3 (PDF: 33–0664) detected in P-1, and only γ-Fe_2O_3 (PDF: 39–1346) in P-3, while P-2 contains α-Fe_2O_3 and γ-Fe_2O_3 phases simultaneously. Calculated with Scherer equation [33] based on 35.6˚ peak, the particle size is 32.2 nm (P-1), 17.7 nm (P-2) and 16.3 nm (P-3), respectively. The data indicates that the particle size in the precursor built by γ-Fe_2O_3 is small.

Fig 2 is the XRD patterns of catalyst C-1, C-2 and C-3. The Fe_2O_3 phases in them are the same as their precursors. The different crystal phases of Fe_2O_3 influence the distribution of promoter Zn, K and Cu in C-1, C-2 and C-3. CuO (PDF: 48–1548) is found in C-1, while $CuFe_2O_4$ (PDF: 25–0283) appears in C-2 and C-3. The dispersion of Cu in C-1 is lower than C-2 and C-3. The existing state of Cu is related to the particle size of Fe_2O_3 in the precursors. Because the Fe_2O_3 size of P-2 and P-3 is only about half of P-1, the dispersed degree of iron atom in P-2 and P-3 is much higher than P-1. The impregnated copper atom can contact with more iron atom in P-2 and P-3 than P-1, which is able to explain why $CuFe_2O_4$ was formed in

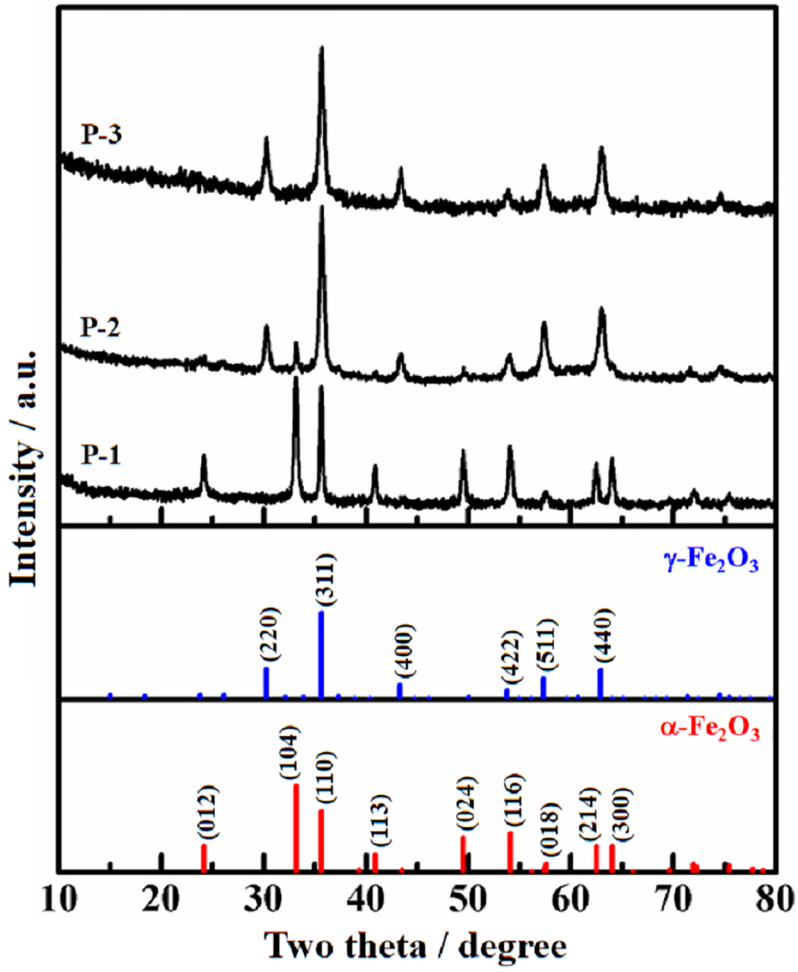

Fig 1. XRD patterns of the precursors, as well as the standard data for α-Fe_2O_3 and γ-Fe_2O_3.

https://doi.org/10.1371/journal.pone.0182955.g001

C-2 and C-3. Although the crystal containing Zn and (or) K is not detected in Fig 2, the existence of Zn and K in the catalysts is confirmed by XPS analysis.

Texture of the precursors and catalysts

Table 1 lists the BET surface area and pore distribution of the precursors and catalysts measured by N_2-adsorption at liquid nitrogen temperature. For the precursors, the specific surface area of P-2 and P-3 is bigger than P-1, which can partly explained by the particle size of Fe_2O_3 in them. Small particle usually constitutes a collective with large surface area. However, the specific surface area of P-3 is less than P-2 regardless of the particle size in P-3 (16.3 nm) is smaller than P-2 (17.7 nm). This contradiction can be solved by the fact that the theoretical densities of γ-Fe_2O_3 (5.47 g·cm^{-3}) is higher than α-Fe_2O_3 (5.27 g·cm^{-3}) [28]. According to Fig 1, P-2 is a mixture of α-Fe_2O_3 and γ-Fe_2O_3, while P-3 is composed of pure γ-Fe_2O_3. As a result, the volume per unit mass of P-2 is larger than P-3. It means that P-2 is in looser state than P-3. Both of the average pore diameter and pore volume are in the order of P-1 > P-2 > P-3.

After the precursors was promoted, the specific surface area and pore volume of C-1, C-2 and C-3 are decreased except the pore volume of C-3. There are two possible factors responsible for the changes. Water, used as solvent in the impregnation of promoters, is the first one.

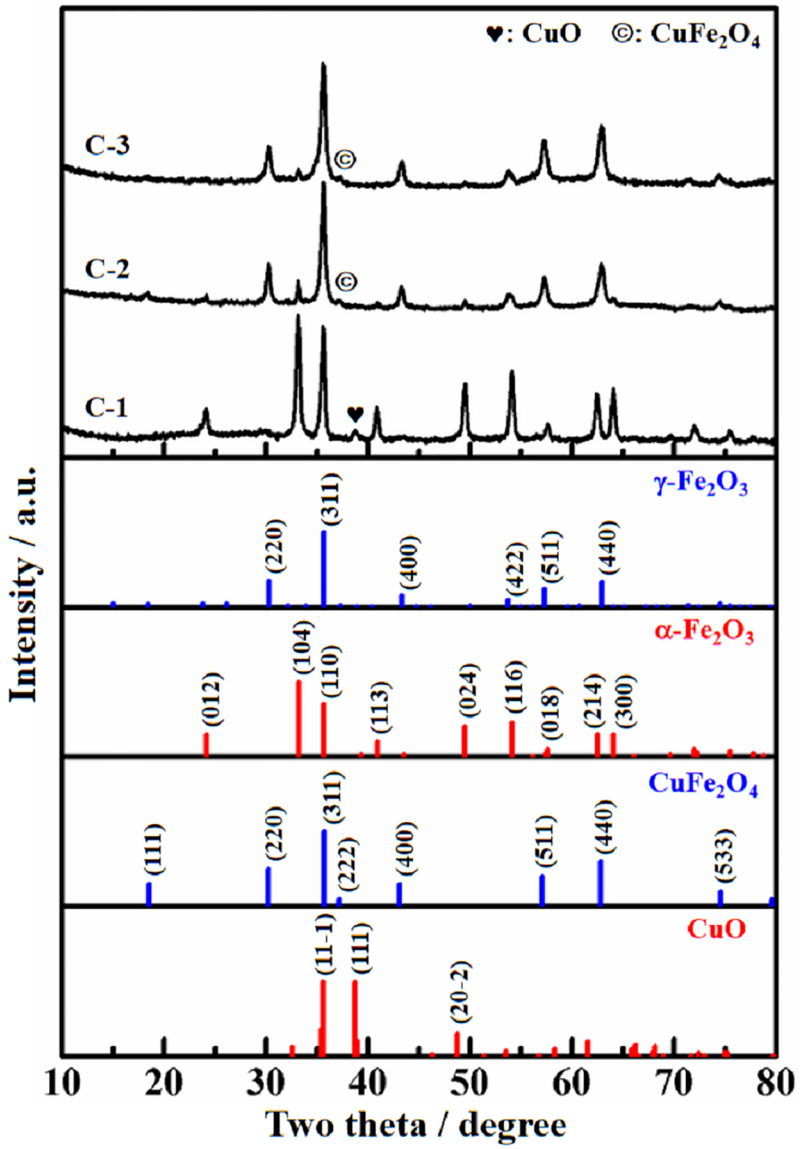

Fig 2. XRD patterns of the catalysts, as well as the standard data for CuO, $CuFe_2O_4$, α-Fe_2O_3 and γ-Fe_2O_3.

https://doi.org/10.1371/journal.pone.0182955.g002

Table 1. Texture of the precursors and catalysts.

Sample	BET surface area (m^2/g)	Average pore diameter (nm)	Pore volume (mL/g)
P-1	32.4	20.6	0.17
P-2	60.2	9.7	0.15
P-3	55.1	5.8	0.06
C-1	19.6	29.0	0.14
C-2	34.6	14.2	0.12
C-3	30.0	11.6	0.09

https://doi.org/10.1371/journal.pone.0182955.t001

Because water has high surface tension, pore structure, especially in small diameter, is destroyed when intrapore water is removed by drying [34]. It makes the loss of catalyst surface area. The second one is the distribution of promoter K in the catalysts. The radius of K^{1+} (1.33 Å) is two times of Fe^{3+} (0.64 Å). The impregnated K mainly distributes on the catalyst surface. It shrinks pore mouth, and even blocks off minor pores in catalyst. Thus, N_2 molecule is prevented to enter into the inner of these pores in the experiment of N_2 adsorption at low temperature. It results in small measured surface area and pore volume [32,35,36]. The morphologies of precursors and catalysts are shown in S1 Fig. There are large particles laying on C-1, which are confirmed to be K-containing particles by EDS (S2 Fig). The blocking to minor pores induces enlarged average pore diameter of the catalysts. S1 Fig also display that the surface of P-3 was fluffed after promoter impregnation, which is possible to induce abnormal increased pore volume of C-3.

XPS characterization

Fig 3 gives the binding energy of Fe 2p in the precursors. The peaks of Fe 2p 3/2 and 2p 1/2 appears at 711.12 eV and 724.75 eV for the three precursors, respectively. The peak intensity of P-2 and P-3 is stronger than P-1, disclosing that the Fe quantity exposed on the surface of P-2 and P-3 is more than P-1. The deduction is supported by the results in Fig 1. The calculated particle size in P-1 is the largest among the three precursors. It results in the lowest surface content of Fe in P-1.

The XPS results of catalyst C-1, C-2 and C-3 are shown in Fig 4. By comparing the peak area of element Fe, K, Cu and Zn, the dispersity of Fe and K on C-2 and C-3 surface is higher than C-1. On the contrary, Cu and Zn are more dispersive on C-1 than C-3. There is no signal of Cu and Zn for C-2. Promoter K mainly distributed on catalyst surface because of its large radius (1.33 Å for K^{1+} ion). From Table 1, the surface areas of C-2 and C-3 are bigger than C-1. It increases the ratio of Fe and K distributed on the catalyst surface. The radius of Zn^{2+} and

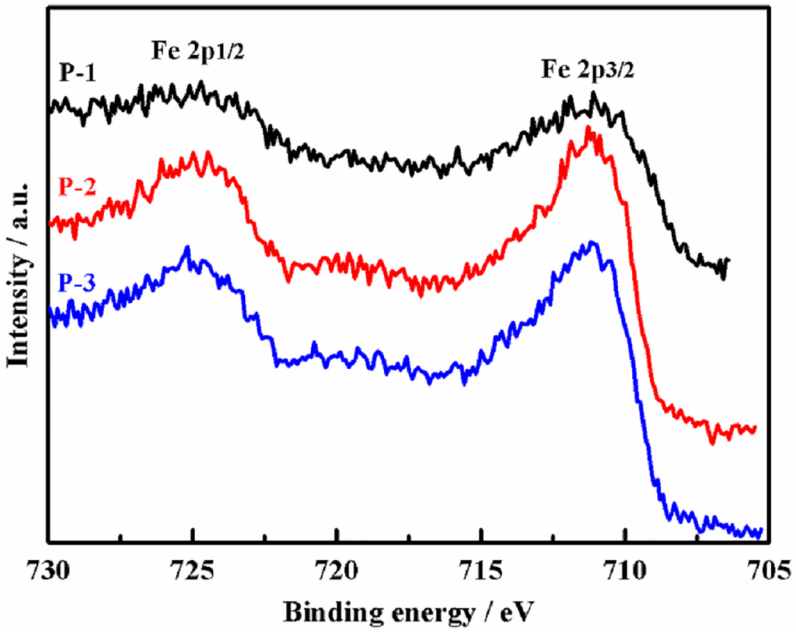

Fig 3. XPS spectrum of element Fe on the precursors.

https://doi.org/10.1371/journal.pone.0182955.g003

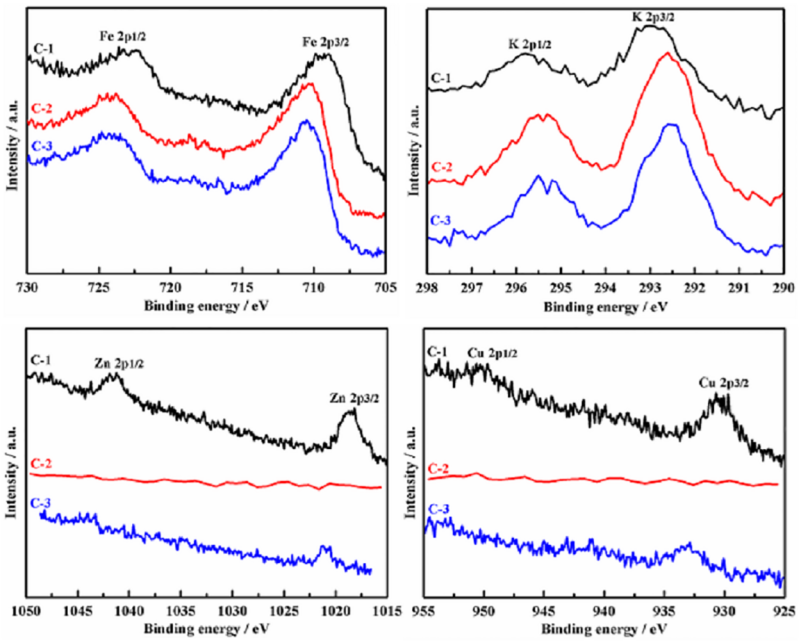

Fig 4. XPS spectra of element Fe, K, Zn and Cu on the catalysts.

https://doi.org/10.1371/journal.pone.0182955.g004

Cu^{2+} is 0.74 Å and 0.72 Å, respectively. They are close to Fe^{3+} (0.64 Å). Therefore, promoter Zn and Cu can enter into the cation vacancy or replace Fe^{3+} in crystal Fe_2O_3. Because γ-Fe_2O_3 is more disorder than α-Fe_2O_3, it makes the inset of Cu and Zn into γ-Fe_2O_3 easier than α-Fe_2O_3. That is why the peak areas of Cu 2p and Zn 2p of C-3 are smaller than C-1. Due to the inserted Cu and Zn surrounded or interacted with much oxygen atom in C-3, their binding energies would be increased relative to C-1 which is reflected by the blue shift of Cu and Zn binding energy. C-2 is a mixture of γ-Fe_2O_3 and α-Fe_2O_3, and the mismatching between the two crystal phases produced much defective sites in C-2. Such disorder structure is beneficial to hold Cu and Zn in the bulk of catalysts. The assumption is supported by the observation of none of Cu 2p and Zn 2p signals for C-2 in Fig 4. Compared with the binding energy of Fe 2p 3/2 of the three precursors, the values of the three catalysts are decreased in the order of C-3 ≈ C-2 < C-1. Dry et al. [37] reported that K donates electrons to Fe. Therefore, a stronger electron shift from K to Fe happened in C-1 than C-2 and C-3.

H_2-TPR

Fig 5 displays the reducibility of the three precursors. The peak temperature corresponding to $Fe_2O_3 \rightarrow Fe_3O_4$ reduction is 340˚C for P-1, while it is around 310˚C for P-2 and P-3 [38,39]. Because γ-Fe_2O_3 is similar to Fe_3O_4 in view of their crystal structure [28,40], γ-Fe_2O_3 is more easily reduced to Fe_3O_4 than α-Fe_2O_3. The weak peak at 350˚C in P-3 is the reduction of α-Fe_2O_3 which was produced from meso-stable γ-Fe_2O_3. The peak corresponding to the reduction of $Fe_3O_4 \rightarrow$ α-Fe is about 550˚C for P-2 and P-3, but 574˚C for P-1 [38,39].

Fig 6 presents the reducibility of the three catalysts. The wild peak below 350˚C in C-1 is assigned to the reduction of $CuO \rightarrow Cu^0$ [32]. The data in Figs 2 and 4 disclose that Cu is highly dispersed into C-2 and C-3. Therefore, there is no evident reduction peak of CuO species for C-2 and C-3. A weak peak around 270˚C appears in C-3 rather than C-2 is consistent with the observed Cu signal in C-3 and none in C-2 (Fig 4). The impregnated promoters

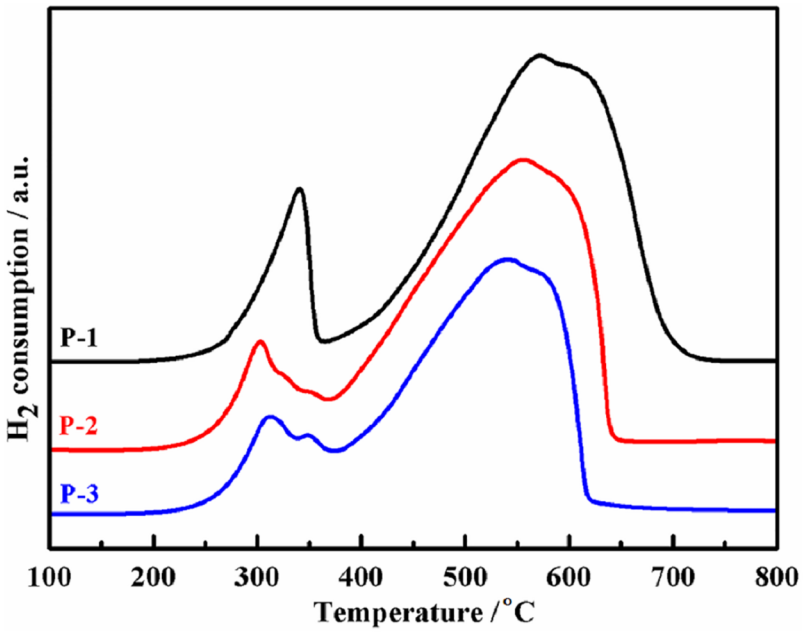

Fig 5. H_2-TPR profiles of the precursors.

https://doi.org/10.1371/journal.pone.0182955.g005

usually induces shrunk surface area as shown in Table 1 [32,35,36]. It leads to decreased Fe dispersity and difficult reduction of iron oxides. Compared with the reduction behavior of the precursors in Fig 5, the corresponding process happened at higher temperature for the catalysts. For C-1, the H_2-consumption peak at 420˚C is from $Fe_2O_3 \rightarrow Fe_3O_4$, and the wild peak centered at 570˚C is assigned to $Fe_3O_4 \rightarrow$ α-Fe. The should peak around 680˚C is the

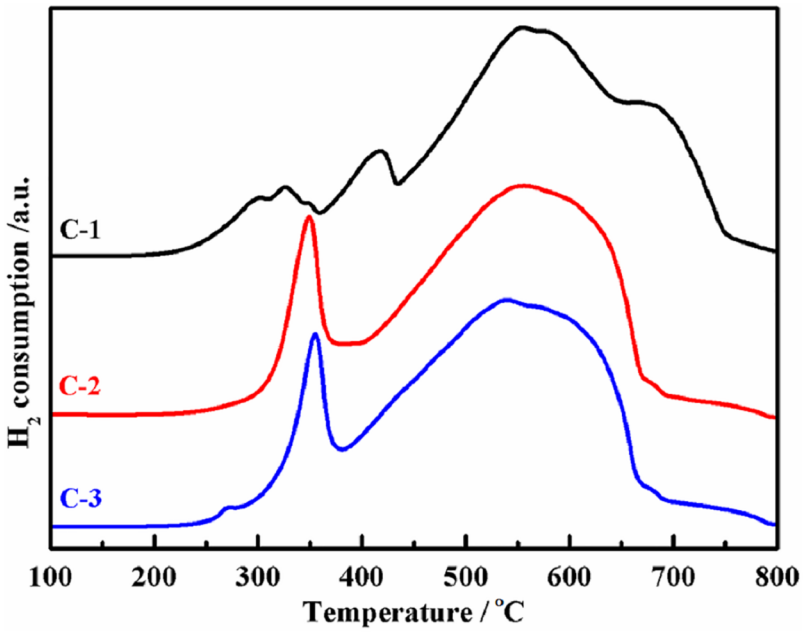

Fig 6. H_2-TPR profiles of the catalysts.

https://doi.org/10.1371/journal.pone.0182955.g006

Table 2. Reactive performance of the catalysts.

Catalyst	CO_2 conv. (%)	Product distribution (C mol. %)			
		CO	CH_4	C_{2-4}	C_5+
C-1	10.4	38.1	13.1	17.7	31.1
C-2	13.2	27.0	11.0	21.1	40.9
C-3	15.1	23.4	10.1	19.5	47.0

1.6 MPa, 230˚C, 6 L/(h·g-cat.), $H_2/CO_2 = 2$

https://doi.org/10.1371/journal.pone.0182955.t002

reduction of Fe_3O_4 covered by K-containing particles as shown in S1 Fig. K can inhibit the reduction of iron oxide by CO [41] and H_2 [35]. The reduction process of iron oxides in C-2 and C-3 are almost same. The peak around 350˚C are from highly dispersive $Cu^{2+} \rightarrow Cu^0$ and $Fe_2O_3 \rightarrow Fe_3O_4$. The wide peak of H_2 consumption in 370˚C—660˚C are from $Fe_3O_4 \rightarrow$ α-Fe. The peak temperature of C-2 and C-3 is about 558˚C and 537˚C, respectively. H_2-TPR results disclose that C-2 and C-3 are easily reduced relative to C-1.

Catalyst performance in CO_2 hydrogenation

The influence of Fe_2O_3 crystal phases on CO_2 hydrogenation is compared in Table 2. The catalytic activity (CO_2 conversion) is proportional to the content of γ-Fe_2O_3 phase in the catalysts. C-3, composed of pure γ-Fe_2O_3 phase, is more active than C-1 which is composed of α-Fe_2O_3. Because C-2 contains α-Fe_2O_3 and γ-Fe_2O_3 simultaneously, its activity is between C-1 and C-3. The higher iron dispersity (Fig 4) and reducibility (Fig 6) of γ-Fe_2O_3 phase is beneficial to form more active site on C-2 and C-3 for CO_2 hydrogenation than C-1, which results in the activity sequence of C-3 > C-2 > C-1.

In view of CO selectivity, it declines with the increased content of γ-Fe_2O_3 phase in the catalysts. The selectivity of total hydrocarbons increases in the order of C-1 < C-2 < C-3. Especially, C-3 is the most active among the three catalysts to synthesize C_5+ hydrocarbons. Promoter K is beneficial for CO_2 hydrogenated into hydrocarbons [15] by inhibited H_2 adsorption [20] and enhanced formation rates of C_2+ hydrocarbons [42]. Although the nominal content of K is same for the three catalysts, Fig 4 unveils that the surface content of K on C-2 and C-3 is higher than C-1. The segregation of promoter K on C-2 and C-3 is responsible for the increased selectivity of hydrocarbons, because the surface atoms are the effective ones to influence the reaction.

Conclusions

The crystal phase of Fe_2O_3 influences the catalyst reactivity in CO_2 hydrogenation by two effects. The first effect is that the dispersity of both Fe and K on the catalyst in γ-Fe_2O_3 phase is higher than the catalyst in α-Fe_2O_3 phase. The second effect is that the catalyst in γ-Fe_2O_3 phase is more easily reduced than the one in α-Fe_2O_3 phase. The catalyst with high dispersive and easily reduced iron oxide can form much active site for CO_2 hydrogenation and the high dispersive promoter K can increase the selectivity of C_2+ hydrocarbons.

Aiming to reinforce the conclusion that γ-Fe_2O_3 phase is better than α-Fe_2O_3 phase to the Fe catalyst for CO_2 hydrogenation, we are trying to prepare catalysts with similar specific surface area which are in α-Fe_2O_3 or γ-Fe_2O_3 phase, respectively. By studying such kind of catalysts, the effect of Fe_2O_3 crystal phases could be understand directly.

Supporting information

S1 Fig. The morphologies of precursors and catalysts observed by SEM. Every sample was observed under three levels of magnification.
(PDF)

S2 Fig. Elements distribution on catalyst C-1 observed by EDS.
(PDF)

Author Contributions

Funding acquisition: Wensheng Ning.

Investigation: Tianqi Wang, Hongxian Chen, Xiazhen Yang, Yangfu Jin.

Methodology: Wensheng Ning.

Supervision: Wensheng Ning.

Writing – original draft: Wensheng Ning.

Writing – review & editing: Wensheng Ning.

References

1. Hardy DR, Coffey T. Process and system for producing synthetic liquid hydrocarbon fuels, U.S. Patent 7420004, B2, 2008.
2. Willauer HD, DiMascio F, Hardy DR, Lewis MK, Williams FW. Development of an electrochemical acidification cell for the recovery of CO_2 and H_2 from seawater. Ind Eng Chem Res. 2011; 50: 9876–9882.
3. Willauer HD, DiMascio F, Hardy DR, Lewis MK, Williams FW. Development of an electrochemical acidification cell for the recovery of CO_2 and H_2 from seawater II. Evaluation of the cell by natural seawater. Ind Eng Chem Res. 2012; 51: 11254–11260.
4. Willauer HD, DiMascio F, Hardy DR, Williams FW. Feasibility of CO_2 extraction from seawater and simultaneous hydrogen gas generation using a novel and robust electrolytic cation exchange module based on continuous electrodeionization technology. Ind Eng Chem Res. 2014; 53: 12192–12200.
5. Wang W, Wang S, Ma X, Gong J. Recent advances in catalytic hydrogenation of carbon dioxide. Chem Soc Rev. 2011; 40: 3703–3727. https://doi.org/10.1039/c1cs15008a PMID: 21505692
6. Saeidi S, Amin NAS, Rahimpour MR. Hydrogenation of CO_2 to value-added products—A review and potential future developments. J CO_2 Util. 2014; 5: 66–81.
7. Lan BY, Shi HF. Review of systems for photocatalytic conversion of CO_2 to hydrocarbon fuels. Acta Phys-Chim Sin. 2014; 30: 2177–2196.
8. Drab DM, Willauer HD, Olsen MT, Ananth R, Mushrush GW, Baldwin JW, et al. Hydrocarbon synthesis from carbon dioxide and hydrogen: A two-step process. Energy Fuels. 2013; 27: 6348–6354.
9. Nozaki F, Sodesawa T, Satoh S, Kimura K. Hydrogenation of carbon dioxide into light hydrocarbons at atmospheric pressure over Rh/Nb_2O_5 or Cu/SiO_2-Rh/Nb_2O_5 catalyst. J Catal. 1987; 104: 339–346.
10. Lee MD, Lee JF, Chang CS. Hydrogenation of carbon-dioxide on unpromoted and potassium-promoted iron catalysts. Bull Chem Soc Jpn. 1989; 62: 2756–2758.
11. Schild C, Wokaun A, Koeppel RA, Baiker A. CO_2 hydrogenation over Nickei/Zirconia catalysts from amorphous precursors: On the mechanism of methane formation. J Phys Chem. 1991; 95: 6341–6346.
12. Williams KJ, Boffa AB, Salmeron M, Bell AT, Somorjai GA. The kinetics of CO_2 hydrogenation on a Rh foil promoted by titania overlays. Catal Lett. 1991; 9: 415–426.
13. Ando H, Xu Q, Fujiwara M, Matsumura Y, Tanaka M, Souma Y. Hydrocarbon synthesis from CO_2 over Fe-Cu catalysts. Cata. Today. 1998; 45: 229–234.
14. Jun KW, Roh HS, Kim KS, Ryu JS, Lee KW. Catalytic investigation for Fischer–Tropsch synthesis from bio-mass derived syngas. Appl Catal A. 2004; 259: 221–226.
15. Riedel T, Claeys M, Schulz H, Schaub G, Nam SS, Jun KW, et al. Comparative study of Fischer–Tropsch synthesis with H_2/CO and H_2/CO_2 syngas using Fe- and Co-based catalysts. Appl Catal A. 1999; 186: 201–213.

16. Zhang Y, Jacobs G, Sparks DE, Dry ME, Davis BH. CO and CO_2 hydrogenation study on supported cobalt Fischer–Tropsch synthesis catalysts. Catal Today. 2002; 71: 411–418.
17. Rohde MP, Unruh D, Schaub G. Membrane application in Fischer-Tropsch synthesis to enhance CO_2 hydrogenation. Ind Eng Chem Res. 2005; 44: 9653–9658.
18. Song C. Global challenges and strategies for control, conversion and utilization of CO_2 for sustainable development involving energy, catalysis, adsorption and chemical processing. Catal Today. 2006; 115: 2–32.
19. Ning W, Koizumi N, Yamada M. Researching Fe catalyst suitable for CO_2-containing syngas for Fischer-Tropsch synthesis. Energy Fuels. 2009; 23: 4696–4700.
20. Dorner RW, Hardy DR, Williams FW, Willauer HD. K and Mn doped iron-based CO_2 hydrogenation catalysts: Detection of $KAlH_4$ as part of the catalyst's active phase. Appl Catal A. 2010; 373: 112–121.
21. Al-Dossary M, Ismail AA, Fierroa JLG, Bouzid H, Al-Sayari SA. Effect of Mn loading onto MnFeO nanocomposites for the CO_2 hydrogenation reaction. Appl Catal B. 2015; 165: 651–660.
22. Dorner RW, Hardy DR, Williams FW, Willauer HD. C_2-C_{5+} olefin production from CO_2 hydrogenation using ceria modified Fe/Mn/K catalysts. Catal Commun. 2011; 15: 88–92.
23. Satthawong R, Koizumi N, Song C, Prasassarakich P. Light olefin synthesis from CO_2 hydrogenation over K-promoted Fe–Co bimetallic catalysts. Catal Today. 2015; 251: 34–40.
24. Mattia D, Jones MD, O'Byrne JP, Griffiths OG, Owen RE, Sackville E, et al. Towards Carbon-Neutral CO_2 conversion to hydrocarbons. ChemSusChem 2015; 8: 4064–4072. https://doi.org/10.1002/cssc.201500739 PMID: 26564267
25. Wei J, Ge Q, Yao R, Wen Z, Fang C, Guo L, et al. Directly converting CO_2 into a gasoline fuel. Nature Commun. 2017; 8: 15174. https://doi.org/10.1038/ncomms15174 PMID: 28462925
26. Albrechta M, Rodemercka U, Schneidera M, Bröring M, Baabe D, Kondratenko EV. Unexpectedly efficient CO_2 hydrogenation to higher hydrocarbons over non-doped Fe_2O_3. Appl Catal B. 2017; 204: 119–126.
27. Li S-S, Li W-J, Jiang T-J, Liu Z-G, Chen X, Cong H-P, et al. Iron oxide with different crystal phases (α- and γ-Fe_2O_3) in electroanalysis and ultrasensitive and selective detection of lead(II): An advancing approach using XPS and EXAFS. Anal Chem. 2016; 88: 906–914. https://doi.org/10.1021/acs.analchem.5b03570 PMID: 26639029
28. Zhu W, Winterstein J, Maimon I, Yin Q, Yuan L, Kolmogorov AN, et al. Atomic structural evolution during the reduction of α-Fe_2O_3 nanowires. J Phys Chem C. 2016; 120: 14854–14862.
29. Apte SK, Naik SD, Sonawane RS, Kale BB. Synthesis of nanosize-necked structure α- and γ-Fe_2O_3 and its Photocatalytic Activity. J Am Ceram Soc. 2007; 90: 412–414.
30. Liu C, Yang S, Ma L, Peng Y, Hamidreza A, Chang H, et al. Comparison on the performance of α-Fe_2O_3 and γ-Fe_2O_3 for selective catalytic reduction of nitrogen oxides with ammonia. Catal Lett. 2013; 143: 697–704.
31. Ma HQ, Zhang JY, Tan X, Zhang L, Wang RJ, Zhang BF. Study on the preparation of Fe-based high temperature shift catalyst by Mössbauer spectroscopy I. The phase transformation of different iron oxide precursors. Chin J Catal. 1995; 16: 365–370.
32. Chen HX, Ning WS, Chen CH, Zhang T. Influence of Fe_2O_3 crystal phase on the performance of Fe-based catalysts for CO_2 hydrogenation. J Fuel Chem Technol. 2015; 43: 1387–1392.
33. Keyvanloo K, Mardkhe MK, Alam TM, Bartholomew CH, Woodfield BF, Hecker WC. Supported iron Fischer—Tropsch catalyst: Superior activity and stability using a thermally stable silica-doped alumina support. ACS Catal. 2014; 4: 1071–1077.
34. Scherer GW. Theory of drying. J Amer Ceram Soc. 1990; 73: 3–14.
35. Yang Y, Xiang HW, Xu YY, Bai L, Li YW. Effect of potassium promoter on precipitated iron-manganese catalyst for Fischer–Tropsch synthesis. Appl Catal A. 2004; 266: 181–194.
36. Ning W, Shen H, Jin Y, Yang X. Effects of weak surface modification on Co/SiO_2 catalyst for Fischer-Tropsch reaction. PLoS ONE. 2015; 10: e0124228 https://doi.org/10.1371/journal.pone.0124228 PMID: 25938725
37. Dry ME, Shingles T, Boshoff LJ, Oosthuizen GJ. Heats of chemisorption on promoted iron surfaces and the role of alkali in Fischer-Tropsch synthesis. J Catal. 1969; 15: 190–199.
38. Wan H, Wu B, An X, Tao Z, Li T, Xiang H, et al. Structural properties, reduction and carburization behaviors of Fe/Cu/K/Al_2O_3 catalyst for Fischer-Tropsch synthesis. Acta Phys-Chim Sin. 2007; 23: 1151–1156.
39. Ning W, Yang X, Yamada M. Influence of palladium on the hydrocarbon distribution of Fischer-Tropsch reaction over precipitated iron catalyst. Curr Catal. 2012; 1: 88–92.

40. Genuzio F, Sala A, Schmidt T, Menzel D, Freund HJ. Phase transformations in thin iron oxide films: Spectromicroscopic study of velocity and shape of the reaction fronts. Surf Sci. 2016; 648: 177–187.

41. Ning WS, Koizumi N, Yamada M. Improvement of promoters on the Fischer–Tropsch activity of mechanically mixed Fe catalysts. Catal Commun. 2007; 8: 275–278.

42. Dictor RA, Bell AT. Fischer-Tropsch synthesis over reduced and unreduced iron oxide catalysts. J Catal. 1986; 97: 121–136.